Title

In vivo macromolecular crowding is differentially modulated by aquaporin 0 in zebrafish lens: Insights from a nanoenvironment sensor and spectral imaging

Journal

Science Advances, 8(7)

ISSN

2375-2548

Authors

Vorontsova, Irene
Vallmitjana, Alexander
Torrado, Belén
et al.

Publication Date

2022-02-18

DOI

10.1126/sciadv.abj4833

Peer reviewed

BIOPHYSICS

In vivo macromolecular crowding is differentially modulated by aquaporin 0 in zebrafish lens: Insights from a nanoenvironment sensor and spectral imaging

Irene Vorontsova[1,2,3]†, Alexander Vallmitjana[4]†, Belén Torrado[4], Thomas F. Schilling[2], James E. Hall[1], Enrico Gratton[4], Leonel Malacrida[5,6]*

Macromolecular crowding is crucial for cellular homeostasis. In vivo studies of macromolecular crowding and water dynamics are needed to understand their roles in cellular physiology and fate determination. Macromolecular crowding in the lens is essential for normal optics, and an understanding of its regulation will help prevent cataract and presbyopia. Here, we combine the use of the nanoenvironmental sensor [6-acetyl-2-dimethylaminonaphthalene (ACDAN)] to visualize lens macromolecular crowding with in vivo studies of aquaporin 0 zebrafish mutants that disrupt its regulation. Spectral phasor analysis of ACDAN fluorescence reveals water dipolar relaxation and demonstrates that mutations in two zebrafish aquaporin 0s, Aqp0a and Aqp0b, alter water state and macromolecular crowding in living lenses. Our results provide in vivo evidence that Aqp0a promotes fluid influx in the deeper lens cortex, whereas Aqp0b facilitates fluid efflux. This evidence reveals previously unidentified spatial regulation of macromolecular crowding and spatially distinct roles for Aqp0 in the lens.

INTRODUCTION

Solutes occupy 35 to 95% of eukaryotic cell volume, with the rest being water. The ratio and interaction between water and solutes determine cellular macromolecular crowding, a key feature of cellular organization and function (*1*–*3*). However, its physiological roles remain obscure and are challenging to study in living organisms. There has been a great effort to understand the roles of macromolecular crowding in enzymatic activity, cell physiology, and pathophysiology, primarily using in vitro and cell culture systems (*1*, *3*–*5*). More recently, crowding has been suggested to stabilize the LPR6 (Low-density lipoprotein receptor-related protein 6) signalosome by linking extracellular physical properties and intracellular signaling (*6*). Moreover, modification of extracellular crowding has been shown to modulate liquid-liquid separation–dependent YAP (Hippo/Yes-associated protein) signaling (*7*). However, efforts to study macromolecular crowding in vivo with noninvasive, high-resolution spectroscopic tools remain challenging. In this study, we were able to overcome the technical difficulties of studying the in vivo development of macromolecular crowding in the ocular lens, as well as testing the contribution of the zebrafish aquaporin 0 (AQP0) orthologs to macromolecular crowding by using a nanoenvironmental sensor 6-acetyl-2-dimethylaminonaphthalene (ACDAN) paired with hyperspectral imaging and spectral phasor analysis.

The ocular lens relies on high macromolecular crowding to determine its structure and function (*8*). To achieve and maintain the required refractive index gradient, the lens fiber cells are enriched with crystallin proteins (*4*). Moreover, lens water is tightly regulated to maintain lens homeostasis and proper optics. Regulation of water transport/activity is finely tuned in different parts of the lens, adjusting macromolecular crowding to optimize the gradient of refractive index (*9*). Water influx/efflux is required to facilitate the microcirculation of ions by inward fluid flow at the lens poles and efflux of nutrients and waste at the equator (*10*). In addition, the direction of fluid and ion transport reverse with depth into the lens because of changes in electrochemical gradients (*11*). Net fluid influx in the inner lens cortex must equal net fluid efflux in the outer cortex to maintain homeostasis (*12*). The mechanisms by which water transport regulates macromolecular crowding in the lens in vivo remain unclear; nonetheless, AQP0 [also known as membrane intrinsic protein (MIP) and MIP26] and, in mammals, aquaporin 5 were proposed as water transport regulators (*13*, *14*). AQP0 is the most abundant membrane protein in the lens and is required for lens homeostasis (*8*). AQP0 permeates water in vitro (*15*) and functions as an adhesive protein (*16*, *17*), cytoskeletal anchor (*18*, *19*), and regulator of gap junctions in lens fiber cells (*20*, *21*). In mammals, a single AQP0 protein performs all of these functions. In contrast, zebrafish (*Danio rerio*), because of an ancient teleost-lineage genome duplication, have two *AQP0* orthologs (*22*), *aqp0a* and *aqp0b*, allowing genetic dissection of at least some of these functions (*23*–*25*). Aqp0a and Aqp0b are both essential for lens transparency at 3 days post fertilization (dpf), but from 4 dpf onward, obvious cataract disappears (*23*–*25*). While the loss of Aqp0b alone causes no apparent lens defects thereafter throughout development, loss of Aqp0a disrupts the anterior lens suture, leading to anterior polar opacity at adult stages (*23*, *26*). Both Aqp0a and Aqp0b expressed in *Xenopus laevis* oocytes permeate water in vitro (*24*, *27*). However, only Aqp0a-deficient, but not Aqp0b-deficient zebrafish required introduction of Aqp0 with intact water transport function to rescue embryonic cataract (*25*), possibly by recovering macromolecular crowding homeostasis.

Measuring water homeostasis in living lenses in the presence or absence of Aqp0 function in specific lens regions is challenging because of the dearth of noninvasive tools. Our approach to investigating water homeostasis in vivo uses a solvatochromic molecule (ACDAN) and hyperspectral imaging to provide information on spectroscopic macromolecular crowding at the nanoenvironment

[1]Physiology and Biophysics, University of California, Irvine, Irvine, CA, USA. [2]Developmental and Cell Biology, University of California, Irvine, Irvine, CA, USA. [3]Neurobiology and Behavior, University of California, Irvine, Irvine, CA, USA. [4]Biomedical Engineering, University of California, Irvine, Irvine, CA, USA. [5]Departamento de Fisiopatología, Hospital de Clínicas, Facultad de Medicina, Universidad de la República, Montevideo, Uruguay. [6]Advanced Bioimaging Unit, Institut Pasteur of Montevideo and Universidad de la República, Montevideo, Uruguay.
*Corresponding author. Email: lmalacrida@pasteur.edu.uy
†These authors contributed equally to this work.

sensor. ACDAN is a nontoxic membrane-permeable fluorescent probe, which reports on water dipolar relaxation (DR) within a few angstroms of its location (*28*, *29*). This probe has been used as a sensor for water dynamics in living cells (*30*, *31*). DR is responsive to macromolecular crowding because of its extreme sensitivity to the number of water molecules and the DR time in its nanoenvironment (see schematic in Fig. 1A). In this study, we define a DR index using hyperspectral microscopy and spectral phasor analysis. Changes in ACDAN DR index are indicative of macromolecular crowding variation. This index was built using spectral phasor plot analysis (*32*, *33*). The spectral phasor transforms spectra pixel-by-pixel into a two-dimensional (2D) scatter plot where the axes are the real and imaginary components of the Fourier transform. This transformation captures the morphology of the emission spectra and maps it onto the phasor 2D space where, in polar coordinates, the angle carries the information regarding the spectral center of mass and the radial direction carries information on the spectral broadening. The spectral phasor properties are crucial for the pixel-by-pixel modelless analysis of the spectral information (*34*), as described in Materials and Methods.

To tackle the spatial/temporal DR information in the lens, we developed a combination of hyperspectral imaging and image processing tools for 3D ($x/y/\lambda$) to 5D ($x/y/z/\lambda/t$) analysis to noninvasively study the development of lens macromolecular crowding and its perturbation in zebrafish Aqp0 mutant lenses. In this work, ACDAN's DR index was first shown to be sensitive to crystallin crowding in vitro and then macromolecular crowding in living zebrafish lenses, validating its utility for measuring water dynamics in vivo. ACDAN imaging in embryonic and larval lenses reveals spatial changes in macromolecular crowding throughout development. The macromolecular crowding revealed by ACDAN within the lens was higher than could be achieved in vitro crystallin samples. We show that the water transport functions of Aqp0a and Aqp0b are required for the normal development of macromolecular crowding in the lens cortex at 4 dpf. Putting these data in light of previous work, we provide evidence that Aqp0a facilitates water influx in the inner lens cortex, whereas Aqp0b promotes fluid efflux in the outer lens cortex. The water transport role of Aqp0b is likely compensated by Aqp0a in *aqp0b*$^{-/-}$, which look like *wild type* (*WT*) but is revealed in double *aqp0a*$^{-/-}$/*aqp0b*$^{-/-}$ mutant lenses as extensive cortical fiber cell swelling. These data provide evidence for spatially distinct regulation of water transport of Aqp0a and Aqp0b in establishing and maintaining regional lens macromolecular crowding.

RESULTS

Spectral imaging of ACDAN reveals macromolecular crowding in vitro

ACDAN spectral imaging provides a readout of environmental DR within a few angstroms of its macromolecular environment (Fig. 1A). Since water is the most abundant dipole-active molecule within cells, interactions with macromolecules can be detected by changes in the ACDAN fluorescence spectrum, resulting in a continuum of water DR that ultimately gives a readout of water concentration (water/solute ratio) and the water activity in the ACDAN nanoenvironment (*31*). Water activity refers to sensing water with different rotational times, including water that interacts with molecules (confined water), when its relaxation is compromised when compared to bulk water (nanosecond versus picosecond relaxation time, respectively) (*34*). In the excited state, ACDAN experiences an increase in its dipole moment, which produces reorganization of the nearby dipole-active molecules leading to DR (*35*). This process is observed as a spectral shift toward longer wavelengths (red shift) in the maximum of the fluorescence emission. To measure these wavelength shifts in the emission, we used hyperspectral imaging, collecting the entire ACDAN spectrum and then transforming to phasor space to map the pixels onto the spectral phasor plot (Fig. 1B) (*34*). A solution of ACDAN in water has a peak fluorescence emission in the green region of the spectrum, around 520 nm, which shifts toward blue (shorter wavelengths) with an increasing protein-to-water ratio (Fig. 1B). The phasor transform's power relies on its fit-free approach, meaning a priori knowledge of the spectral emission characteristics is not required.

ACDAN has previously been used to study changes in macromolecular crowding in yeast (*30*, *36*) and HeLa cells (*31*). However,

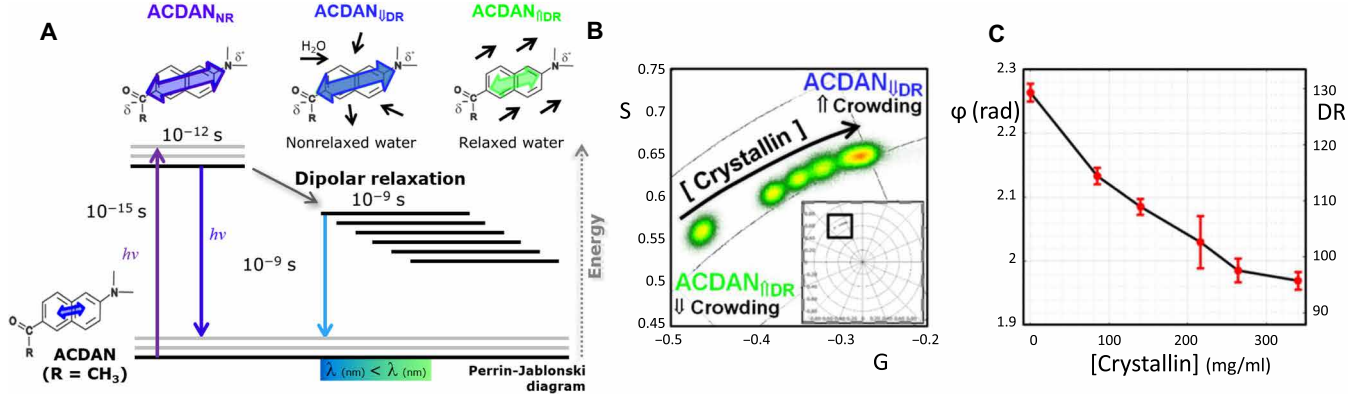

Fig. 1. Solvatochromic properties of ACDAN measure water homeostasis and macromolecular crowding. (**A**) ACDAN photophysics display strong sensitivity to the polarity of the environment and solvent relaxation. In an uncrowded environment, high DR results in a spectral red shift, while in crowded environments, low DR results in a spectral blue shift. (**B**) Phasor plot of spectral emission of ACDAN in solutions containing Antarctic tooth fish γM8d crystallin at concentrations of 0, 85, 140, 216, 264, and 340 mg/ml. A blue spectral shift is observed in response to increased macromolecular crowding. Inset shows complete spectral phasor space with region of interest marked with the black square. (**C**) The mean phasor phase angle/DR show an inverse relationship with crystallin concentration ($n = 3$). The DR scale was extended above 100 (right-hand vertical axes extends to 130) to include the spectral shift found at the crystallin solutions, while lens DR was in the 0 to 100 range.

the ocular lens has some of the highest concentrations of protein of any tissue in the body (*8*), largely crystallins. Thus, we first tested the spectral emission responses of ACDAN to increasingly crowded conditions caused by the Antarctic tooth fish ɣM8d crystallin concentrations in solution. Consistent with ACDAN serving as an accurate quantitative readout of the water activity (confinement) and, therefore, protein-water ratio, we observed a blue spectral emission shift (DR decrease) as crystallin concentration increased (Fig. 1B), confirming its sensitivity to macromolecular crowding in a lipid-free environment. Figure 1C shows the phase shift due to the decrease in DR when the concentration of ɣM8d crystallin increases from 0 to 340 mg/ml, which is close to maximum crystallin solubility. Note that short shifts of ACDAN in the delta phase represent substantial increases in macromolecular crowding.

Macromolecular crowding increases during lens development

We developed an automated image processing pipeline to analyze hyperspectral stacks acquired from zebrafish lenses (Fig. 2A). The details of this experimental pipeline can be found in fig. S1. To study lens spatial DR, ACDAN spectra were transformed pixel by pixel into the spectral phasor plot (Fig. 2B), and then, following the reciprocity principle, the DR value for each pixel (color scale) was applied back to its original *x*-*y* location (Fig. 2C). To further analyze regional lens DR, images were segmented into different lens regions, measuring the distribution of DR across the radial geometry of the lens (Fig. 2D and fig. S2), and *z*-stacks were carried out. This analysis is fundamental to understand the spatiotemporal DR during lens development and growth. 3D geometry (fig. S3) and the axial DR (covered in the following sections) were then reconstructed from these images.

Crystallins are by far the most abundant cytoplasmic lens proteins. They become more concentrated toward the lens center, generating the gradient of refractive index required for emmetropia. We visualized DR during the formation of this gradient in the zebrafish lens in vivo using ACDAN. The ACDAN signal was analyzed in embryonic and larval lenses in the equatorial plane. Since fish grow at different rates depending on their environment, lens diameters and age were used as measures of development during analysis (fig. S4A), as we previously used (*37*).

ACDAN intensity alone in images does not provide valuable information in terms of water activity despite changes in the probe quantum yield. However, the transformation of the hyperspectral data into phasor plots reveals a clear map of the water DR (fig. S5). By using the reciprocity principle of the phasor transformation, it is possible to generate a macromolecular crowding map at subcellular resolution in the lens. The phasor clouds obtained for the different stages (fig. S5, B1 to B6) are blue-shifted (lower phase) with respect to the higher crystallin concentration (340 mg/ml) obtained in vitro (Fig. 1, B and C). This result indicates that higher macromolecular crowding is experienced by ACDAN within lens cells.

In the immature lens at 2 dpf, a high DR signal was found in the lens core, as well as likely in cell nuclei in the lens cortex and nucleus (Fig. 3A1). Higher DR in the cell nuclei compared to the cytoplasm has been previously observed in cell culture and indicates lower nuclear macromolecular crowding. At 2 dpf, fiber cell nuclei are prominent and dispersed through the nucleus of the lens (*23*, *38*). Although by 3 dpf, cell nuclei and organelles in fiber cells of the lens nucleus are degraded as part of the maturation of the lens (*26*, *38*), the highest DR signal, which was in the cytoplasm of fiber cells, was still in the center of the lens, compared to lower DR at the lens periphery (Fig. 3A2). As the lens matured, the lens nucleus gradually decreased in DR, and the maximum DR signal moved to the lens cortex, indicating an increased macromolecular crowding in the lens nucleus (Fig. 3, A3 to A5). The smooth mean radial profile confirmed the shift of the mean DR signal from the lens nucleus (r/a = 0) in young lenses to the cortex in older/larger lenses (Fig. 3B). The maximum DR signal stabilized at a relative distance from the lens center of $r/a \sim 0.7$ from around 5 dpf and older (Fig. 3C). A sigmoid curve was used to model the transition between the two states, and the fit to this curve was very high (R^2 = 0.94). Regionally segmented DR showed a decrease in DR signal in the inner cortex (Fig. 3D4) and more so in the lens nucleus with development (Fig. 3D5).

Regions 5 to 10 μm and 85 to 140 μm from the anterior pole (see table S1) were imaged to determine changes in DR as anterior and posterior sutures formed (Fig. 4), respectively. DR decreased slightly

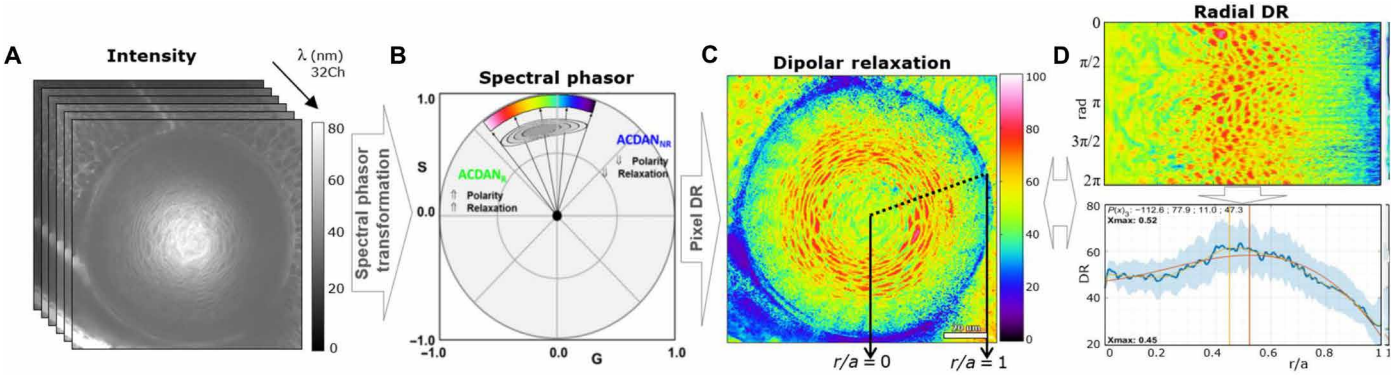

Fig. 2. Characterization of lens ACDAN emission using the phasor approach. (**A**) Hyperspectral images were transformed to the spectral phasor plot (**B**), which separates signal from relaxed and unrelaxed dipolar states. (**C**) DR values were applied back to the original image pixel by pixel, which were then processed for parameter extraction. (**D**) Radial analysis of mean DR signal from the center of the lens (r/a = 0), to lens periphery (r/a = 1) is shown, where r is the distance from lens center and a is the lens radius. The polar geometry is transformed to Cartesian geometry, with the horizontal direction being the radius and the vertical direction being the angle, and the mean DR value is then graphed (bottom), enabling analysis of regional change of mean DR. A polynomial fit was used to estimate max DR. Details can be found in fig. S2.

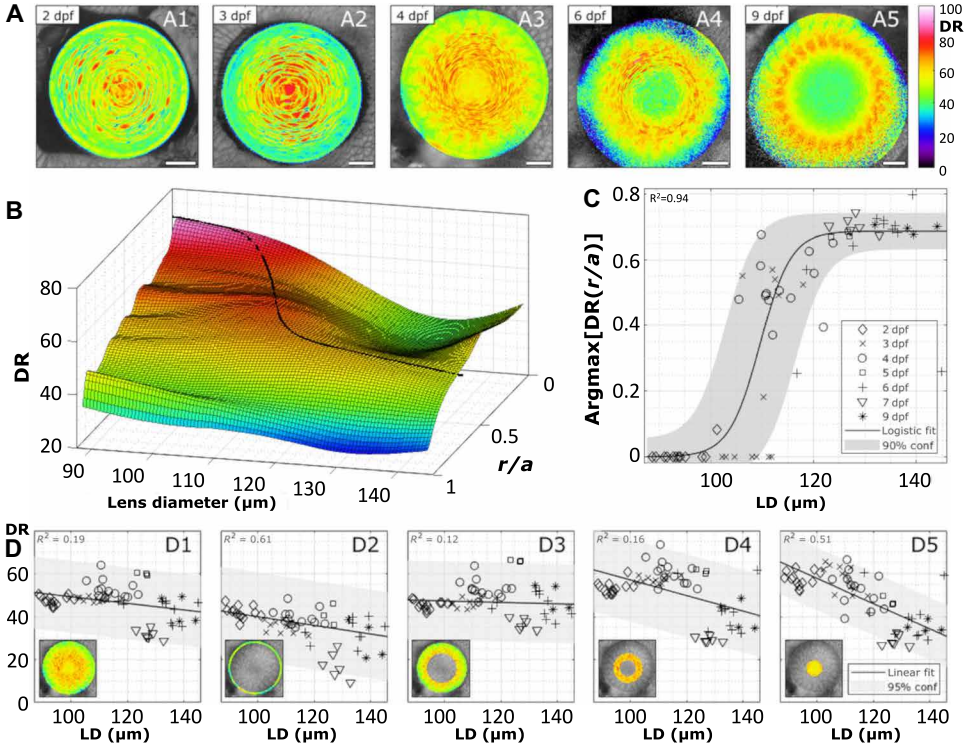

Fig. 3. Distribution of DR in equatorial planes of zebrafish lenses during development. (**A**) Examples of DR images of lenses at specified dpf. Scale bars, 20 µm. (**B**) Smoothed surface of the mean DR radial profile (*r*/*a*) as a function of lens diameter (LD) ($n = 63$), where *r* is the distance from lens center and *a* is the lens radius. (**C**) Radial lens position of the maximal DR value with development. The data are fit to a sigmoid and, in turn, represented on the surface in (B). (**D**) Mean DR of the whole equatorial lens plane (D1), the epithelium (D2), outer cortex (D3), inner cortex (D4), and nucleus (D5) of the lens as indicated by the insets. See table S2 for a summary of *n* numbers. See fig. S5 for ACDAN intensity images, spectral phasor plots, and DR images for examples shown in (A).

in anterior sutures with lens development (Fig. 4B4), while the lens epithelium (Fig. 4B2) and cortex (Fig. 4B3) DR were unchanged. The mean DR in anterior planes overall appeared similar at all stages, while the max DR slightly shifted away from the deeper cortex with development (fig. S6, A and B). DR at posterior poles initially increased from 2 to 4 dpf and then decreased in older lenses (Fig. 4, C and D). This trend was particularly apparent in the posterior suture (Fig. 4D3). These trends were verified by a mean DR smoothed surface plot and maximum DR plot (fig. S6, C and D). Posterior regions had higher DR compared to the anterior regions (fig. S7 A1, B1, and C1).

Imaging *z*-stacks of several lenses further confirmed these DR patterns. Examples of 2 to 4 dpf lens *z*-stacks in equatorial and axial orientations are provided as movies S1 to S6. To confirm that the DR patterns observed in mature lenses were not artifacts of the optical setup (e.g., low in the center and high at the periphery), spherical and conical slicing of the *z*-stacks was performed. Spherical slices were obtained as described for the equatorial, anterior, and posterior planes by measuring the mean radial DR profile for each of the planes in the *z*-stack. We then obtained the DR distribution for each of these planes. The same procedure was performed in conical sections at different angles from the center of the lens to obtain the DR profile for each cone. By finding the maximum DR using the polynomial fit described previously and plotting it for the two spatial distributions, it is evident that the radial position of the maximum remains constant for the conical slices but not for the parallel slices, proving that the geometry is spherical (fig. S3). This analysis confirmed that the observed DR patterns were an intrinsic property of the lens and were not artifacts.

Loss of Aqp0a function regionally disrupts macromolecular crowding in the lens

To understand the roles of Aqp0a and Aqp0b in lens water homeostasis and, therefore, macromolecular crowding, spatial studies of DR were carried out in null mutants previously generated by CRISPR-Cas9 gene editing (*23*). We focused on 4 dpf, as this stage follows loss of organelles from the lens nucleus and embryos have hatched, but the signal from the lens is still strong and not obscured by lens density and peripheral eye structures. Furthermore, our DR analysis during lens development showed that DR is lower in the nucleus compared to the cortex at 4 dpf, suggesting maturation of the macromolecular crowding and likely lens optics. See fig. S8 for ACDAN intensity images to DR transformation data. Equatorial images of ACDAN emission revealed uniformly lower DR in *aqp0a*$^{-/-}$ mutant lenses (Fig. 5A2) compared with *WT* (Fig. 5A1) and swollen cells with high DR, particularly in the cortex in double *aqp0a*$^{-/-}$/*aqp0b*$^{-/-}$ mutant lenses (Fig. 5A4). Furthermore, double *aqp0a*$^{-/-}$/*aqp0b*$^{-/-}$ mutant lenses had increased diameters (fig. S4B), while the other three genotypes were indistinguishable, indicating that the whole lens in double *aqp0a*$^{-/-}$/*aqp0b*$^{-/-}$mutants swelled. In contrast, DR levels and distribution in *aqp0b*$^{-/-}$ mutants (Fig. 5A3) appeared very similar to *WT* (Fig. 5A1), with lower DR in the nucleus and elevated DR more peripherally. Mean DR values as a function of lens depth confirmed that *aqp0a*$^{-/-}$ mutant lenses had a lower DR,

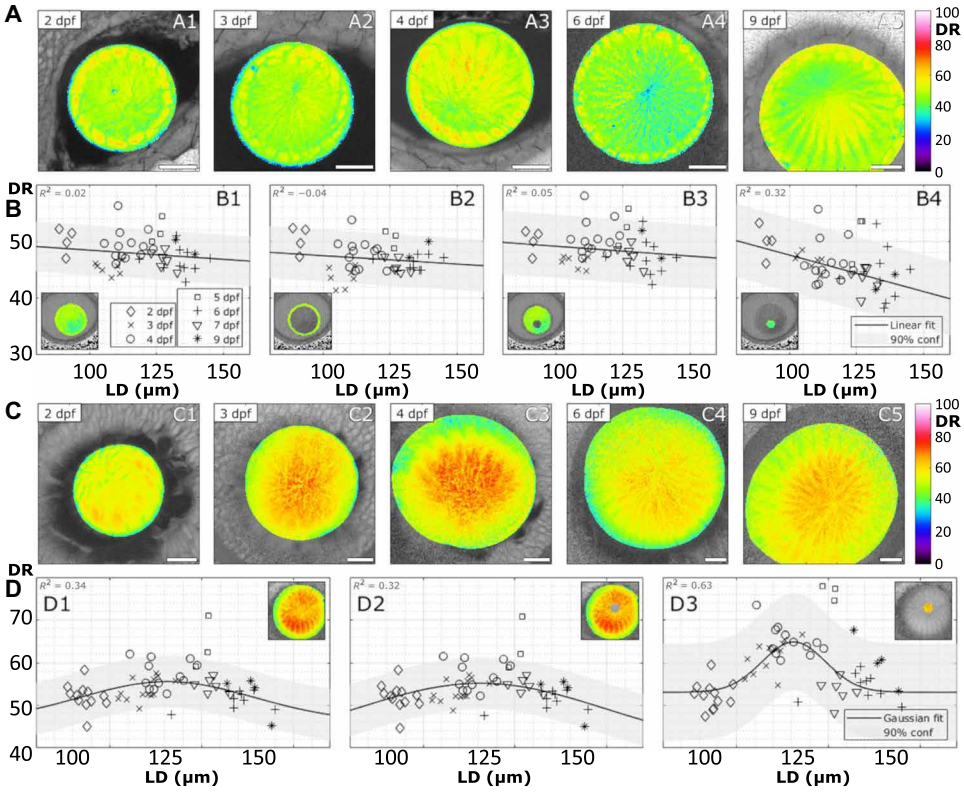

Fig. 4. Distribution of DR in anterior and posterior planes of zebrafish lenses during development. (**A**) Examples of DR images of lenses obtained at the anterior pole at specified dpf. Scale bars, 20 μm. (**B**) Mean DR of the whole anterior lens plane (B1), the epithelium (B2), fiber cells (B3), and sutural region (B4) as indicated by the insets ($n = 45$). (**C**) Examples of DR images of lenses obtained at the posterior pole at specified dpf. Scale bars, 20 μm. (**D**) Mean DR of the whole posterior lens plane (D1), fiber cells (D2), and sutural region (D3; $n = 59$). See table S2 for a summary of n numbers.

particularly in the cortex, compared to other genotypes ($r/a > 0.4$; Fig. 5B). There was variability in phenotype penetrance in double *aqp0a*$^{-/-}$/*aqp0b*$^{-/-}$ mutant lenses (fig. S9), as previously observed (*23*). However, double mutant lenses had higher mean DR in the outer cortex compared to *WT* and *aqp0a*$^{-/-}$ mutant lenses ($r/a > 0.6$; Fig. 5B), and the maximum DR value was closer to the lens periphery (Fig. 5C). Analyses of masked regions of the lens confirmed that the epithelium and cortex of *aqp0a*$^{-/-}$ mutant lenses, but not the lens nucleus, had a lower DR than *WT* (Fig. 5D) when measured at these equatorial planes.

We next examined the lens poles (see table S1 for specific locations). At the anterior pole, we have previously shown that *aqp0a*$^{-/-}$ mutants show severe anterior suture defects at older stages (*23*). ACDAN emission analysis in anterior lens planes revealed that *aqp0a*$^{-/-}$ mutant lenses had lower DR (Fig. 6A2) than other genotypes, which were all quite similar to one another (Fig. 6, A1, A3, and A4). This lower DR in *aqp0a*$^{-/-}$ compared to the other genotypes was confirmed by comparison of the mean DR of the fiber cells (Fig. 6B3), including the suture (Fig. 6B4). In contrast, cells in the epithelium showed no difference (Fig. 6B2 and fig. S10A). The maximum DR signal was closer to the center in *aqp0a*$^{-/-}$/*aqp0b*$^{-/-}$ double mutant lenses than *WT* (fig. S10B).

At the posterior pole, *aqp0a*$^{-/-}$ lenses also exhibited lower DR than other genotypes (Fig. 6C2), while double *aqp0a*$^{-/-}$/*aqp0b*$^{-/-}$ mutant lenses had regions with higher DR that appeared as swollen cells (Fig. 6C4). Cell morphology was severely disrupted in double *aqp0a*$^{-/-}$/*aqp0b*$^{-/-}$ mutant lenses, and these lenses lacked a clear convergence of a suture compared to the other genotypes (Fig. 6, C1 to C3). Statistically, *aqp0a*$^{-/-}$ had a lower DR in the cortex and sutural regions of the posterior cortex compared to the other genotypes, while the double mutant was not statistically different (Fig. 6, D1 to D3). The mean DR was relatively even around the sutures within a radius of ~20 μm, with a dip at the center (fig. S10C), which is likely why the maximum DR was very scattered around this value in all genotypes (fig. S10D). The DR was overall lower in whole lenses, fiber cells, and sutures at the anterior pole compared to the posterior pole in all genotypes (fig. S7).

Reconstructions of *z*-stacks in axial orientations confirmed the DR patterns and phenotypes observed in lenses imaged as single optical slices (Fig. 7). Together, these results suggest that both zebrafish Aqp0s facilitate fluid efflux, disruption of which leads to lower DR and swollen fiber cells in the lens periphery, but that only Aqp0a facilitates fluid influx, which is required to develop and maintain a higher DR throughout the lens cortex.

Aqp0 requires water transport function to rescue macromolecular crowding defects in Aqp0-deficient lenses

To test whether it is the water transport property of the Aqp0s that is required for establishment and maintenance of lens water homeostasis, we used WT and water-transport-dead Aqp0 DNA constructs and tested their ability to rescue *aqp0a*$^{-/-}$ and double *aqp0a*$^{-/-}$/*aqp0b*$^{-/-}$ mutant lens DR phenotypes. An AQP0 from the killifish

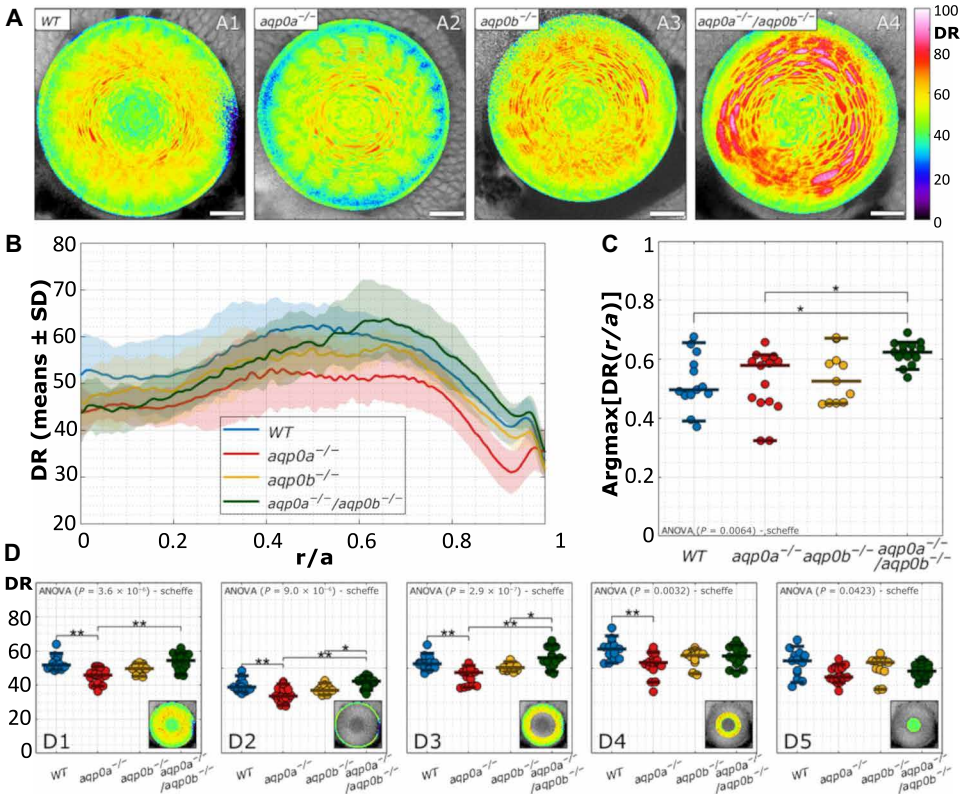

Fig. 5. Disruption of DR distribution in Aqp0 mutant lenses. (**A**) Examples of DR images of lenses at 4 dpf of *WT* and mutants. Scale bars, 20 μm. (**B**) DR radial profiles ($n = 54$). (**C**) Radial lens position of the maximal DR values are shown as function of distance into the lens, where r is the distance from lens center and a is the lens radius. (**D**) Mean DR of the whole equatorial lens plane (D1), epithelium (D2), outer cortex (D3), inner cortex (D4), and nucleus (D5) of the lens as indicated by the insets. See table S3 for a summary of n numbers. See fig. S8 for ACDAN intensity images, spectral phasor plots, and DR images for examples shown in (A). Statistical significance was denoted with * at a significance level $P < 0.05$ and ** at a significance level $P < 0.005$.

(*Fundulus heteroclitis*), MIPfun, was used to rescue DR phenotypes. Transiently expressed MIPfun has previously been shown to rescue embryonic cataract due to knockdown of Aqp0a or Aqp0b. Thus, MIPfun can likely perform the functions of both zebrafish Aqp0s and displays high water permeability similar to the zebrafish Aqp0s, unlike mammalian AQP0 (*24*, *39*). Mosaics with strong expression of the transgenesis marker, mCherry, indicating MIPfun construct integration in lens cells were selected for analysis (Fig. 8B). Variability in the penetrance of mutant phenotypes, especially of the double *aqp0a*$^{-/-}$/*aqp0b*$^{-/-}$mutant (see fig. S9) were further exacerbated by mosaicism of the rescue. Therefore, here, we report the most consistent phenotypes with examples.

Injection of either WT (MIPfun) or a water-channel-dead rescue construct (MIPfunN68Q) into *WT* lenses did not affect the lens DR or morphology (Fig. 8, C2 and C3). *WT* MIPfun rescued the low DR of *aqp0a*$^{-/-}$ (Fig. 7D2), and the high DR of swollen cells in double *aqp0a*$^{-/-}$/*aqp0b*$^{-/-}$ mutant was also less severe (Fig. 7E2). Both transgenics appeared more similar to the uninjected *WT* lens (Fig. 7C1) compared to uninjected mutant lenses (Fig. 7, D1 and E1). MIPfunN68Q failed to rescue the mutant phenotypes and made them more severe (Fig. 7, D3 and E3). This observation confirms that the water transport function of Aqp0a (and Aqp0b when Aqp0a is also missing) are essential for establishing and maintaining lens water homeostasis and the macromolecular crowding environment in the lens cortex.

DISCUSSION

In this study, we apply hyperspectral imaging of the solvatochromic probe ACDAN as an environmental nanosensor to demonstrate the contributions of Aqp0a and Aqp0b to the establishment and maintenance of macromolecular crowding in the living zebrafish lens. Using this novel approach, we first characterized regional development of macromolecular crowding in the lens nucleus from embryonic to larval stages, which correlates with the development of lens optics. Macromolecular crowding increases in the lens nucleus as the lens matures. Water is handled differently during development at the anterior and posterior zebrafish lens sutures, likely the result of regional differences in water influx in early development. Hyperspectral analysis of ACDAN in Aqp0 zebrafish null mutants reveals that Aqp0a is required for the generation and maintenance of a normal distribution of water activity and macromolecular crowding in the lens cortex, probably by water influx in the deeper cortex. A role for Aqp0b in water transport is manifested as swollen cells only in *aqp0a*$^{-/-}$/*aqp0b*$^{-/-}$ double mutants, while lens cells of *aqp0b*$^{-/-}$ mutants alone resemble those of *WT*. The severity of these macromolecular crowding phenotypes were reduced by overexpression of functional Aqp0 from killifish but not by an Aqp0 unable to transport water, confirming the specificity of phenotypes resulting from loss of water transport function. These data are consistent with previous studies suggesting divergent functions for the two zebrafish Aqp0s, with Aqp0a playing a key role in water transport in the lens

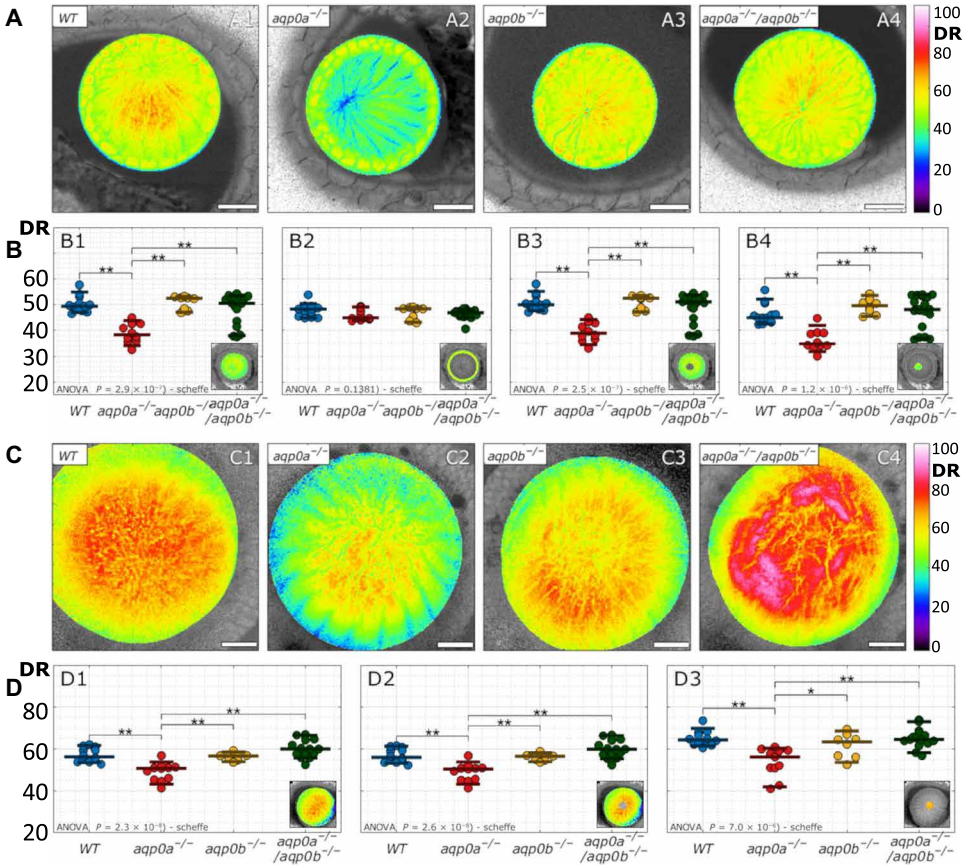

Fig. 6. DR in anterior and posterior planes of Aqp0 mutant lenses. (**A**) Examples of DR images were taken at anterior planes (10 μm from the anterior pole) of lenses at 4 dpf. Scale bars, 20 μm. (**B**) Mean DR of the whole anterior lens plane (B1), the epithelium (B2), fiber cells (B3), and sutural regions (B4) as indicated by the insets ($n = 50$). (**C**) Examples of DR images taken at posterior planes of lenses (75 to 85 μm from the anterior pole). Scale bars, 20 μm. (**D**) Mean DR of the whole posterior pole (D1), fiber cells (D2), and sutural region (D3) as indicated by the insets ($n = 46$). See table S3 for a summary of n numbers. Statistical significance was denoted with * at a significance level $P < 0.05$ and ** at a significance level $P < 0.005$.

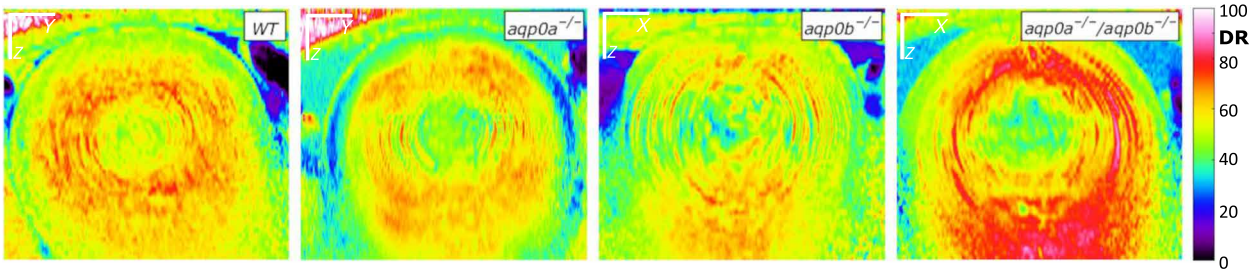

Fig. 7. Axial orientation of DR signal in Aqp0 mutant lenses. Examples of DR axial slices through the center of the lens in *WT*, *aqp0a*$^{-/-}$, *aqp0b*$^{-/-}$, and *aqp0a*$^{-/-}$/*aqp0b*$^{-/-}$ double mutant lenses reconstructed from *z*-stacks. Anterior is oriented up. Scale bars, 20 μm.

that can also compensate for the loss of Aqp0b. Although Aqp0b has other important functions in lens fiber cells, particularly adhesion (*40*), we demonstrate that it can also contribute to water transport under certain conditions. We provide a model for how these findings add to the current understanding of water transport in facilitating fiber cell growth and lens development, as well as for maintaining lens homeostasis in the context of the microcirculation of fluid (Fig. 9).

Our primary finding is that DR in the lens (regardless of developmental stage; Fig. 3) is lower than the most concentrated crystallin solution (Fig. 1C). In absolute units, the lowest water DR obtained for ACDAN in living lenses was ~30 DR, which is much lower when compared to ~95 DR found in the most concentrated crystallin solution (340 mg/ml). This result indicates that the water in the interior of the lens cells is more confined and gel-like than water even in concentrated protein solutions (*41*, *42*). This confirms a higher

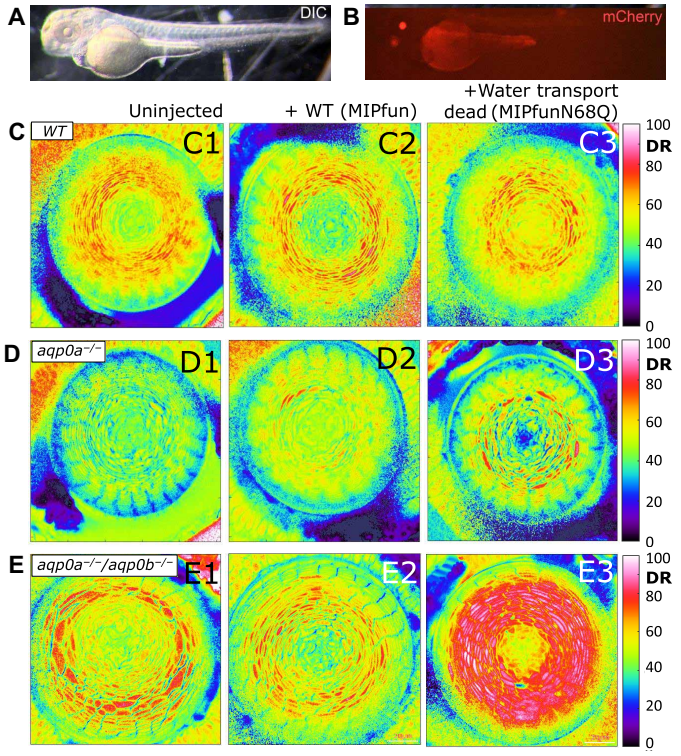

Fig. 8. Water channel dead rescue did not restore water homeostasis in the lens. (**A**) Example of a zebrafish injected with a rescue construct imaged under differential interference contrast (DIC) illumination and (**B**) strong expression of the transgenesis marker, mCherry, in the lens with some autofluorescence from the yolk. Examples of DR images of (**C**) *WT*, (**D**) *aqp0a*$^{-/-}$, and (**E**) *aqp0a*$^{-/-}$/*aqp0b*$^{-/-}$ double mutant 4 dpf lenses in equatorial orientation uninjected and injected with WT MIPfun (*F. heteroclitus* AQP0) rescue construct *Tg(HuβB1cry:MIPfun-IRES-mCherry)*, and water transport dead construct *Tg(HuβB1cry:MIPfunN68Q-IRES-mCherry)*. Representative lenses of at least four experiments are shown.

total concentration of crystallins in the in vivo lens (up to 60% total mass), where aggregation is largely prevented by chaperones (*43*) compared to what can be achieved in solution before crystallin aggregation occurs (*8*). Furthermore, lens cell compaction, cytoskeletal and intermediate proteins, lipids, and other macromolecular crowders required for normal lens refractive properties all contribute to the unique macromolecular environment of the lens. Thus, within the lens, especially the lens nucleus, water is highly confined (low DR activity), limiting the rate of ACDAN relaxation and emphasizing the tight control of macromolecular crowding for fiber cell function and lens optics.

Hyperspectral imaging of ACDAN from embryonic to larval stages revealed progressively lower DR signal in the lens nucleus compared to the cortex, consistent with previous evidence of nuclear fiber cell compaction and concentration of crystallins as part of lens maturation (*37*). These changes lead to an increase in the protein-to-water ratio in the lens nucleus, contributing to the development of the appropriate refractive index for a functional visual system around 3.5 dpf (*44*), to allow larval zebrafish to use vision in feeding and evading predators by 5 dpf. Interesting differences were observed in the DR signal between the anterior and posterior regions of the lens. DR peaked in the posterior lens cortex and suture around 4 to 5 dpf and then dropped at older stages (Fig. 4). In contrast, anterior sutures showed slightly decreased DR with development, likely indicating tightening of the sutures. The high DR at the posterior pole likely reflects the posterior position of the zebrafish lens germinal zone at embryonic and larval stages (*45*, *46*) compared with mammalian lenses with high water influx into the rapidly elongating and growing differentiating fiber cells. As lenses mature, the germinal zone shifts anteriorly toward the center of the lens along the optical axis, correlated with a reduced DR at the posterior pole. Newly formed sutures then tighten, likely leading to low DR at both poles.

In addition to water, macromolecular crowding is affected by pH, ion concentration, and electrochemical gradients. In mature mammalian lenses, pH decreases (*47*), intracellular Na^+ (*48*) and Ca^{2+} (*49*) concentrations increase, hydrostatic pressure increases (*50*), and the plasma membranes depolarize from ~−70 to ~−30 mV as a function of lens depth from the periphery to the center of the lens nucleus (Fig. 9A) (*10*). These regional physiological differences and spatially localized transporters and channels facilitate the microcirculation of ions and fluid in the lens. The microcirculation system is the leading hypothesis for the maintenance of mammalian lens homeostasis facilitating nutrient entry and waste removal in the largest avascular tissue in the body [reviewed by Donaldson *et al.* (*12*)]. A net influx of ions and fluid occurs at the poles and travels along the sutures and extracellular spaces between cells, with ions then entering cells via ion transporters or channels creating an osmotic water influx through aquaporins. Net ion and fluid efflux occur in the outer cortex localized at the lens equator. While such lens microcirculation has not yet been demonstrated directly in the zebrafish, it is likely to be conserved, especially at older stages when lens size is more similar to that of the mouse/young rat lens.

Using ACDAN, we characterized the development of DR during the stages when lenses acquire these unique characteristics. Most notable is the decrease in DR in the lens nucleus with development, with the maximum DR shifting to the cortex (see Fig. 3). This shift in the DR maximum is evident at 4 dpf (lens diameter ~100 to 120 μm). At 3 dpf, the highest DR was measured in the center of the lens, similar to earlier stages, despite the lens nucleus having lost its organelles by 65 hours after fertilization (*38*), and appearing tightly packed morphologically (*26*, *45*). This high DR index at 3 dpf suggests that water has not yet been extracted from the nucleus, that maximal macromolecular crowding of the lens nucleus has not yet been reached, and that the optics, particularly the index of refraction, are immature. It is likely that by 4 dpf, when we observe a drop in the DR in the lens nucleus, a substantial increase in lens nucleus hydrostatic pressure has been achieved to extrude water from this region, which, in turn, establishes the high macromolecular crowding and water homeostasis required for the optical properties of the lens. This coincides with previous reports of the zebrafish visual system becoming functional around 3.5 dpf (*44*). Future studies will focus on the change in lens DR transition from 3 to 4 dpf in detail to investigate how it is affected by pH, ion concentrations (particularly Ca^{2+}), or electrochemical gradients and to determine when the hydrostatic pressure gradient is established in the zebrafish lens.

On the basis of ACDAN DR analyses of Aqp0 null mutants, we propose a model (Fig. 9) that suggests that both zebrafish Aqp0s facilitate fluid efflux in the peripheral lens cortex, but only Aqp0a facilitates influx in the deeper lens cortex. Since loss of Aqp0a would decrease water influx, this would lead to the intracellular environment of the cortex being more crowded, resulting in lower DR values in all cortical regions. When both Aqp0a and Aqp0b are missing,

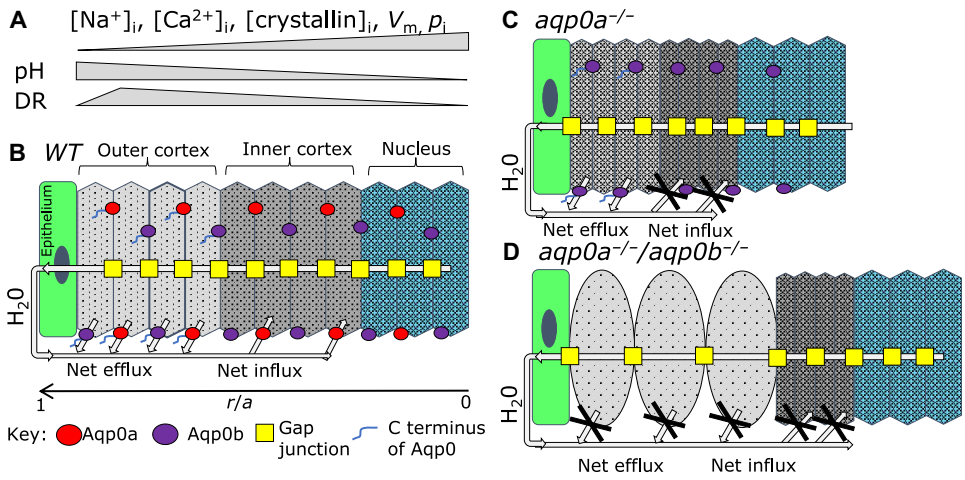

Fig. 9. Model for the roles of Aqp0a and Aqp0b in lens water transport in vivo. (**A**) Summary of physiological changes: intracellular Na^+ ($[Na^+]_i$), Ca^{2+} ($[Ca^{2+}]_i$), crystallin concentrations ($[crystallin]_i$), plasma membrane voltage potential (V_m), lens hydrostatic pressure (p_i), and intracellular pH are shown as relative changes by gray bars, which occur from the outer cortex to the nucleus in a mature lens correlating to lens regions in (B). These changes determine its regional macromolecular crowding and, thus, DR. DR peaks in the outer cortex in mature lenses and decreases in the lens nucleus, indicating that the lowest macromolecular crowding and the highest water activity is in the outer lens cortex and lowest water activity is in the highly crowded lens nucleus. (**B**) Diagram of a mature equatorial lens fiber cell stack from epithelium ($r/a = 1$) to the center of the lens nucleus ($r/a = 0$) with direction of H_20 flow shown on the basis of previously published work. (r is the distance from lens center and a is the lens radius). Aqp0a (red) and Aqp0b (purple) localize to both broad and narrow fiber cell membranes. Analysis of DR in *aqp0a*$^{-/-}$ (C) and *aqp0a*$^{-/-}$/*aqp0b*$^{-/-}$ (D) lenses shows that both Aqp0a and Aqp0b facilitate osmotic water efflux in the outer cortex, while only Aqp0a facilitates water influx into fiber cells in the inner cortex (B). (**C**) Loss of Aqp0a results in a net loss of water influx, but Aqp0b is still able to facilitate efflux, resulting in net loss of water leading to increased macromolecular crowding and lower DR in the outer and inner cortex. (**D**) In double *aqp0a*$^{-/-}$/*aqp0b*$^{-/-}$ mutants, both the H_20 influx and efflux pathways are disrupted. This water loss results in a more crowded environment in the inner cortex with lower crowding in the swollen cells of the outer cortex.

both fluid influx and efflux are disrupted, resulting in cell swelling in the periphery, particularly near the posterior pole, and shrinkage in the deeper cortex. This swelling is marked by high DR in the swollen cells, indicative of lower macromolecular crowding. A role for Aqp0b in water influx appears to be dispensable and compensated by Aqp0a, as *aqp0b*$^{-/-}$ lenses resemble *WT* at 4 dpf. Anterior and posterior poles of *aqp0a*$^{-/-}$ mutants have reduced DR compared to *WT*, indicating a reduced influx throughout the lens cortex (see Fig. 6). Aqp0a water transport function near the poles correlates with sutures and lens nucleus centralization. Loss of water transport functions of Aqp0a in *aqp0a*$^{-/-}$ at older stages likely results in this localized disruption (*23*). In contrast to the cortex, our DR data suggest that Aqp0a and/or Aqp0b are not essential for the maintenance of water homeostasis in the zebrafish lens nucleus, at least at 4 dpf.

Alternatively, the phenotype of the double *aqp0a*$^{-/-}$/*aqp0b*$^{-/-}$ mutant may be due to loss of the adhesion functions of Aqp0b (*40*). However, we find no evidence of extracellular space dilations in the double *aqp0a*$^{-/-}$/*aqp0b*$^{-/-}$ mutant lenses, which we would expect if cell membranes have separated because of loss of cell-to-cell adhesion. Instead, cell swelling is observed. Furthermore, since the lens DR of *aqp0b*$^{-/-}$ mutants resembles *WT* at 4 dpf, it is likely that the loss of its adhesive properties is compensated by other mechanisms, such as gap junctions. Another potential role of Aqp0b, and possibly Aqp0a as well, that might explain these phenotypes could be interactions with two key lens proteins connexin 50 and filensin. It is currently unknown whether zebrafish Aqp0 orthologs also regulate connexin 50 and filensin, as has been shown for mammalian AQP0 (*20*, *21*).

Our rescue experiments provide evidence to support the model that the water transport functions of Aqp0a and Aqp0b are required for proper macromolecular crowding and, by inference, water homeostasis (Fig. 8). We show that WT MIPfun, which likely has functions of both zebrafish Aqp0s, reduces the severity of the DR reduction in *aqp0a*$^{-/-}$ mutants, most likely by restoring water influx in the cortex. WT MIPfun also reduces the severity of cell swelling in double mutants, consistent with restoration of water influx and efflux. In contrast, mutant MIPfun constructs lacking water transport function (MIPfunN68Q) fail to rescue the DR phenotypes in both mutants and exacerbate their severity. The introduction of a nonfunctional form of Aqp0 could be more detrimental than a missing Aqp0, as AQP0 monomers have been shown to work cooperatively in a tetramer (*51*). Thus, the mutant MIPfunN68Q could disrupt the function of the native Aqp0s, exacerbating the phenotype in *aqp0a*$^{-/-}$ or *WT*, by forming heterotetramers in mosaics. However, *WT* appears unaffected with the introduction of MIPfunN68Q, indicating normal water channel function. It is unclear why double mutants lacking both Aqp0a and Aqp0b appear worse with overexpression of MIPfunN68Q since there is no functional Aqp0a or Aqp0b present. Together, these data confirm the essential roles of Aqp0a and Aqp0b as water channels for maintenance of fluid influx/efflux balance in the lens cortex and, thus, overall lens homeostasis due to tight tuning of macromolecular crowding.

It yet remains unclear why there are functionally distinct water transport roles for the two zebrafish Aqp0s, while their spatial and temporal expression in the lens appears to be identical by immunohistochemistry (*23*). It could be due to differences in regulation between the two Aqp0s, as has already been shown for their sensitivity to pH. Aqp0a increases water permeability at higher pH, while Aqp0b increases permeability at lower pH in vitro (*27*). Since pH decreases with depth into the lens, Aqp0b permeability may increase in the deeper lens cortex. However, our DR data suggest that Aqp0a plays the primary role of transporting water into cells in the deeper

cortex, while both paralogs facilitate efflux in the periphery, where pH would be neutral. Another potential permeability regulation difference that could lead to differential activity may be sensitivity to external Ca^{2+}, which is yet to be tested in the two zebrafish Aqp0s.

In conclusion, macromolecular crowding is essential in all living cells, and in this study, we used hyperspectral imaging of the nanoenvironment sensor, ACDAN, to describe the development of macromolecular crowding in the living zebrafish lens at a subcellular level. The combination of spectroscopy tools and imaging processing analysis enabled us to report the very high macromolecular crowding in the lens compared with a high concentration of crystallin in solution. We show that as lens optics develop, DR decreases, indicating increased macromolecular crowding in the lens nucleus from 2 to 6 dpf. We also show that the *aqp0a*$^{-/-}$ mutant lens cortex had reduced macromolecular crowding, while cell swelling was evident in *aqp0a*$^{-/-}$/*aqp0b*$^{-/-}$ double mutant lenses. These results indicate that both zebrafish Aqp0s facilitate fluid efflux in the outer lens cortex, but only Aqp0a facilitates fluid influx in the inner cortex of living zebrafish lenses. In the future, we will test the requirements of amino acids known to regulate Aqp0 water transport by external Ca^{2+} and pH on DR and fluid influx and efflux in the lens cortex. This study also provides tools and methods for studying water dynamics and macromolecular crowding mechanisms in other tissues in living organisms.

MATERIALS AND METHODS

Zebrafish husbandry

The animal protocols used in this study adhered to the ARVO (The Association for Research in Vision and Ophthalmology) Statement for the Use of Animals in Ophthalmic and Vision Research and have been approved by the Institutional Animal Care and Use Committee of University of California, Irvine protocol no. AUP-20-145. Zebrafish (AB strain) were raised and maintained under standard laboratory conditions (*52*), except that methylene blue was excluded from the embryonic media (EM), as this yielded background fluorescence during hyperspectral imaging. The *aqp0a*$^{-/-}$ and/or *aqp0b*$^{-/-}$ mutants were generated as previously described (*23*). 1-phenyl-2-thiourea (0.003%; P7629, Sigma-Aldrich, St Louis, MO) was added to EM from 20 to 24 hours after fertilization to prevent pigment formation. From 6 dpf, larvae were fed a diet of live rotifers (*52*).

Rescue constructs

For rescue of mutant phenotypes, the Tol2 transposable element system (*53*) was used to stably integrate WT *Tg(HuβB1cry:MIPfun-IRES-mCherry)* or water-channel-dead *Tg(HuβB1cry:MIPfunN68Q-IRES-mCherry)* constructs of the *Fundulus heteroclitus* AQP0 (MIPfun). A 200–base pair region of the human βB1 crystallin promoter (*54*) was used to drive expression specifically in the lens, and only lenses strongly expressing the transgenesis marker [internal ribosomal entry site (IRES)–mCherry] were used to assess rescue of the phenotype. By using spectral phasors, we were able to extract ACDAN data without interference from mCherry (*55*), so it was selected as a transgenic marker. Previously, MIPfun had successfully rescued morpholino knockdown–induced transient cataracts at 3 dpf of Aqp0a or Aqp0b, so it is thought to encompass properties of both zebrafish Aqp0s (*25*). MIPfunN68Q mutation results in an inactive water channel aquaporin (*25*) and so was used to test the requirement for water channel function to rescue DR phenotypes.

Crystallin preparation

The Antarctic toothfish (*Dissostichus mawsoni*) γM8d crystallin (GenBank, DQ143983) sample was provided by J. Bierma from R. Martin's laboratory. The recombinant proteins were grown, purified, and stored as previously described (*56*). Dilution series from 0 to 340 mg/ml were made in buffer [10 mM phosphate (pH 6.9), 50 mM NaCl, and 0.05% NaN_3]. Concentration was measured by a NanoDrop at absorbance 280 nm and corrected by $\varepsilon_{280} = 1.063$ ml/mg at 1 nm.

ACDAN staining

ACDAN (A168445, Toronto Research Chemicals, North York, ON, Canada) was dissolved in dimethyl sulfoxide at 67 mM stock concentration and added fresh to EM at a final concentration of 100 μM for overnight incubation of zebrafish before imaging. ACDAN was added at a final concentration of 5 μM 10 min before imaging of the crystallin preparation.

Hyperspectral imaging

Embryos and larvae were anesthetized in EM with 0.0165% (w/v) tricaine (A5040, Sigma-Aldrich, St. Louis, MO) and mounted in 1% low melt agarose (T9284, Sigma-Aldrich, St. Louis, MO) in 35-mm glass bottom microwell dishes (P35G-1.5-14-C, MatTek Corporation, Ashland, MA) with the eye against the coverslip and the optical path perpendicular to the imaging plane (fig. S11). Imaging planes were kept consistent between lenses of specific age as summarized (table S1).

Hyperspectral fluorescence images were acquired using a Zeiss LSM 710 META microscope (Carl Zeiss, Jena GmbH) with a ×40 water immersion objective 1.2 numerical aperture (Carl Zeiss, Jena GmbH). The microscope was coupled to a Ti:Sapphire laser (Spectra-Physics Mai Tai, Newport Beach, CA), which produces 80-fs pulses with a repetition rate of 80 MHz. A two-photon wavelength of 780 nm was used for ACDAN excitation. The average laser power illuminating the sample was maintained at the milliwatt level. Hyperspectral detection was performed with the Lambda Mode configuration of the Zeiss LSM 710 META, which consists of a 32-channel GaAsP array photomultiplier tube. The hyperspectral range collected was from 416 to 728 nm; each of the 32 channels had a bandwidth of 9.7 nm. Image acquisition was performed with a frame size of 1024 × 1024 pixels and a pixel size of 100 nm. Hyperspectral data were processed using a custom routine developed in MATLAB (The Mathworks Inc., Boston, MA), described in the following sections.

Spectral phasor of hyperspectral images

The image processing pipeline that we developed uniquely for analyzing spectral microscopy images of ACDAN emission in the zebrafish eye lenses is based on the spectral phasor transform. This integral transform obtains two quantities (named *G* and *S*) from the spectral intensity distribution at each pixel, which are used to create the phasor plot of an image (*57*). The Cartesian coordinates (*G*, *S*) of the spectral phasor plot are defined by the following expressions

$$G = \frac{\int_{\lambda_0}^{\lambda_f} I(\lambda)\cos(\omega n(\lambda - \lambda_0))\, d\lambda}{\int_{\lambda_0}^{\lambda_f} I(\lambda)\, d\lambda} \quad (1)$$

$$S = \frac{\int_{\lambda_0}^{\lambda_f} I(\lambda)\sin(\omega n(\lambda - \lambda_0))\, d\lambda}{\int_{\lambda_0}^{\lambda_f} I(\lambda)\, d\lambda} \quad (2)$$

where $I(\lambda)$ is the intensity as a function of wavelength at a particular pixel, measured in the interval ($\lambda_0\lambda_f$) that depends on the detector spectral range. The parameter n is the harmonic, i.e., the number of cycles of the trigonometric function that are fit in the wavelength range by means of the angular frequency ω

$$\omega = \frac{2\pi}{\lambda_f - \lambda_0} \tag{3}$$

In practice, one does not have a continuum of intensity values in the spectral direction but rather a discrete number corresponding to the number of detectors that cover the spectral range. For computational purposes, the spectral phasor transform expressed as a discrete transform in terms of the spectral channel is (*58*)

$$G = \frac{\sum_c^{N_c} I(c)\cos(2\pi c/N_c)}{\sum_c^{N_c} I(c)} \tag{4}$$

$$S = \frac{\sum_c^{N_c} I(c)\sin(2\pi c/N_c)}{\sum_c^{N_c} I(c)} \tag{5}$$

where, now, $I(c)$ is the pixel intensity at channel c and N_C is the total number of channels. It is important that even if the number of spectral channels is small (in our case 32), the coordinates S and G are quasi-continuous since the photon counts in each pixel and channel $I(c)$ are high enough (~10^2) to allow a wide range of values in the coordinates S and G.

The spectral phasor position of a particular pixel carries information about the spectral intensity profile of that pixel, allowing us to distinguish minute differences in the spectral emission. In polar coordinates, the angle carries the information regarding the spectral center of mass, and the radial direction carries information on the spectra broadness.

Spectral phasors follow rules of vector algebra, known as the linear combination of phasors (*32*, *59*). This property refers to the additivity of components and allows the geometrical calculation of mixed pure environments. Pixels that contain a combination of two independent fluorescent species will appear on the phasor plot in a position that is a linear combination of the phasor positions of the two independent spectral species. The relative intensity fractions of the components determine the coefficients of the linear combination.

The other crucial property of the phasor plot is known as the reciprocity principle, which refers to the fact that every point on the phasor plot corresponds to a pixel on the image and vice versa, i.e., there is a bidirectional mapping between the image and the points. Note that this operation is not a mathematical inversion; given the coordinates of a pixel in the phasor plot, one cannot recover the photon spectral distribution of that pixel. This reciprocity maintained between the raw data and the phasor space representation allows us to select a region of interest in the phasor plot distribution and display the location of those pixels in the original image. An in-depth description of the properties of spectral phasor plots is given in (*34*, *60*).

The phasor transform applied to each pixel of an image produces a point in the phasor plot, and all the pixels of an image together comprise the phasor plot. In the case of the particular range of wavelengths of our experiments and the range of our spectral detector array, this distribution was in a region between the first and second quadrant of the phasor plot. After plotting all the spectral images in the spectral phasor plot (a total of 420 images), we manually defined our region of interest to include all the points in the phasor plot in terms of a phase angle interval. This phase angle interval [φ_0, φ_f] was chosen at [65°, 115°], which approximately corresponds to the range [470, 520] nm. This interval was then used to define our DR index as follows

$$\mathrm{DR} \equiv 100\frac{\arctan(S/G) - \varphi_0}{\varphi_f - \varphi_0} \tag{6}$$

This quantity was then mapped to a particular lookup table (colormap) to color-code each pixel in the images according to the position of the pixel's phasor transform in this interval [see Fig. 2 (B and C)]. This color-coded image therefore now corresponds to a value in the interval [0,100], in turn, corresponding to the aforementioned angular interval. It is this magnitude that we refer to as the DR index (*35*). This DR definition does not require any prior knowledge of spectral characteristics of the sample.

A special consideration during the image processing steps regards saturated pixels in the images. This circumstance is uncommon since during the acquisition, we ensured the use of a fraction of the dynamic range, but on rare occasions with a few outlier pixels, this condition did not hold. Because, in such pixels, the spectral distribution is capped at some point, an error was introduced in the computation of the phasor transform. For this reason, these pixels were marked before computing the phasor transform, and the G and S phasor values for these pixels were interpolated a posteriori by averaging the neighboring pixels' G and S values.

Image processing routine for spatial/temporal study of the lens

To perform the spatial analysis, lenses were segmented from the background. Since the lenses are not perfectly circular and the challenge to align lenses perfectly to the imaging optical axis and, most importantly, the radial geometry of the cells conforming the lens does not, in general, match with the geometric center of the lens, the segmentation was performed in a semiautomatic way. For each image (420 total images), we manually marked six points around the edge of the lens, which were then used to automatically interpolate an arc joining them while forcing continuity in the arc and its derivative. The central point in the lens was used as the arc anchor, which had also been manually marked. This segmentation allowed tracing a total of 360 radii and obtaining the mean radial DR values in all directions. These curves were then interpolated to have equal numbers of points and were used to construct a Cartesian unfolding of the DR distribution of the lens (fig. S2). From this Cartesian unfolded lens, one direction being the radius and the other being the angle, the mean radial DR profile was obtained by projecting the mean DR in the angular direction (Fig. 2D).

From the original circular geometry, a regional separation was applied to obtain the mean DR in each of the relevant regions of the lens. These regions were defined as annular bands, taking into account the irregular geometry of the lens section, i.e., if the center of the lens is not the geometric center, in one direction, the regional bands are tighter than in the other. For the equatorial plane, a total of four regions were defined: epithelium ($r/a < 0.93$), outer cortex ($0.55 < r/a < 0.93$), inner cortex ($0.30 < r/a < 0.55$), and core ($r/a < 0.30$). For the anterior plane, the epithelium was manually segmented, and both for the anterior and posterior planes, the suture was defined as the central circle of radius 10 μm. The image processing experimental pipeline is represented in fig. S1.

Statistical analysis

When plotting results, we performed several fits to the data points. In such cases, the coefficient of determination (R^2; unity minus the sum of squared distances to the fit over the sum of squared distances to the mean) is provided to measure the goodness of fit of the models used. Furthermore, a shaded area with a chosen confidence interval was also drawn in the background.

When comparing two independent distributions, the one-sided Kolmogorov-Smirnov test for normality was performed in each of the two distributions. In the cases in which the test was passed, a Student's *t* test was used to statistically test whether the data came from normal distributions with equal means. In the cases where the normality test was not passed, the Wilcoxon rank sum test was used to statistically measure the chance that the two sets of points were drawn from distributions with equal medians.

When comparing more than two independent distributions, again, the Kolmogorov-Smirnov test was used to test for normality of each distribution, and in the successful cases, an analysis of variance (ANOVA) test was performed against the hypothesis that all groups are drawn from distribution with equal means. When the normality test failed, the Kruskal-Wallis test was used instead (*61*). In both cases, for further comparison of pairwise distributions for equal means, Scheffe's procedure was chosen, as it proved to be the most conservative.

SUPPLEMENTARY MATERIALS

Supplementary material for this article is available at https://science.org/doi/10.1126/sciadv.abj4833

View/request a protocol for this paper from *Bio-protocol*.

REFERENCES AND NOTES

1. B. Akabayov, S. R. Akabayov, S.-J. Lee, G. Wagner, C. C. Richardson, Impact of macromolecular crowding on DNA replication. *Nat. Commun.* **4**, 1615 (2013).
2. P. Dey, A. Bhattacherjee, Role of macromolecular crowding on the intracellular diffusion of DNA binding proteins. *Sci. Rep.* **8**, 844 (2018).
3. G. Nettesheim, I. Nabti, C. U. Murade, G. R. Jaffe, S. J. King, G. T. Shubeita, Macromolecular crowding acts as a physical regulator of intracellular transport. *Nat. Phys.* **16**, 1144–1151 (2020).
4. M. A. Mourão, J. B. Hakim, S. Schnell, Connecting the dots: The effects of macromolecular crowding on cell physiology. *Biophys. J.* **107**, 2761–2766 (2014).
5. A. A. M. André, E. Spruijt, Liquid–liquid phase separation in crowded environments. *Int. J. Mol. Sci.* **21**, 5908 (2020).
6. Y. Li, M. Chen, J. Hu, R. Sheng, Q. Lin, X. He, M. Guo, Volumetric compression induces intracellular crowding to control intestinal organoid growth via Wnt/β-catenin signaling. *Cell Stem Cell* **28**, 63–78.e7 (2021).
7. D. Cai, D. Feliciano, P. Dong, E. Flores, M. Gruebele, N. Porat-Shliom, S. Sukenik, Z. Liu, J. Lippincott-Schwartz, Phase separation of YAP reorganizes genome topology for long-term YAP target gene expression. *Nat. Cell Biol.* **21**, 1578–1589 (2019).
8. G. J. Wistow, J. Piatigorsky, Lens crystallins: The evolution and expression of proteins for a highly specialized tissue. *Annu. Rev. Biochem.* **57**, 479–504 (1988).
9. P. J. Donaldson, A. C. Grey, B. Maceo Heilman, J. C. Lim, E. Vaghefi, The physiological optics of the lens. *Prog. Retin. Eye Res.* **56**, e1–e24 (2017).
10. R. T. Mathias, J. Kistler, P. Donaldson, The lens circulation. *J. Membr. Biol.* **216**, 1–16 (2007).
11. R. T. Mathias, J. L. Rae, Transport properties of the lens. *Am. J. Physiol. Cell Physiol.* **249**, C181–C190 (1985).
12. P. J. Donaldson, K.-S. N. Chee, J. C. Lim, K. F. Webb, Regulation of lens volume: Implications for lens transparency. *Exp. Eye Res.* **88**, 144–150 (2009).
13. R. S. Petrova, K. F. Webb, E. Vaghefi, K. Walker, K. L. Schey, P. J. Donaldson, Dynamic functional contribution of the water channel AQP5 to the water permeability of peripheral lens fiber cells. *Am. J. Physiol. Cell Physiol.* **314**, C191–C201 (2018).
14. K. Schey, R. Petrova, R. Gletten, P. Donaldson, The role of aquaporins in ocular lens homeostasis. *Int. J. Mol. Sci.* **18**, 2693 (2017).
15. J. E. Hall, J. A. Freites, D. J. Tobias, Experimental and simulation studies of aquaporin 0 water permeability and regulation. *Chem. Rev.* **119**, 6015–6039 (2019).
16. S. S. Kumari, K. Varadaraj, Intact AQP0 performs cell-to-cell adhesion. *Biochem. Biophys. Res. Commun.* **390**, 1034–1039 (2009).
17. Y. Nakazawa, M. Oka, M. Funakoshi-Tago, H. Tamura, M. Takehana, The extracellular C-loop domain plays an important role in the cell adhesion function of aquaporin 0. *Curr. Eye Res.* **42**, 617–624 (2017).
18. Y. Nakazawa, M. Oka, K. Furuki, A. Mitsuishi, E. Nakashima, M. Takehana, The effect of the interaction between aquaporin 0 (AQP0) and the filensin tail region on AQP0 water permeability. *Mol. Vis.* **17**, 3191–3199 (2011).
19. K. M. L. Rose, R. G. Gourdie, A. R. Prescott, R. A. Quinlan, R. K. Crouch, K. L. Schey, The C terminus of lens aquaporin 0 interacts with the cytoskeletal proteins filensin and CP49. *Invest. Ophthalmol. Vis. Sci.* **47**, 1562–1570 (2006).
20. J. Liu, J. Xu, S. Gu, B. J. Nicholson, J. X. Jiang, Aquaporin 0 enhances gap junction coupling via its cell adhesion function and interaction with connexin 50. *J. Cell Sci.* **124**, 198–206 (2011).
21. X. S. Yu, J. X. Jiang, Interaction of major intrinsic protein (aquaporin-0) with fiber connexins in lens development. *J. Cell Sci.* **117**, 871–880 (2004).
22. T. S. Vihtelic, J. M. Fadool, J. Gao, K. A. Thornton, D. R. Hyde, G. Wistow, Expressed sequence tag analysis of zebrafish eye tissues for NEIBank. *Mol. Vis.* **11**, 1083–1100 (2005).
23. I. Vorontsova, I. Gehring, J. E. Hall, T. F. Schilling, Aqp0a regulates suture stability in the zebrafish lens. *Invest. Ophthalmol. Vis. Sci.* **59**, 2869–2879 (2018).
24. A. Froger, D. Clemens, K. Kalman, K. L. Németh-Cahalan, T. F. Schilling, J. E. Hall, Two distinct aquaporin 0s required for development and transparency of the zebrafish lens. *Invest. Ophthalmol. Vis. Sci.* **51**, 6582–6592 (2010).
25. D. M. Clemens, K. L. Nemeth-Cahalan, L. Trinh, T. Zhang, T. F. Schilling, J. E. Hall, In vivo analysis of aquaporin 0 function in zebrafish: Permeability regulation is required for lens transparency. *Invest. Ophthalmol. Vis. Sci.* **54**, 5136–5143 (2013).
26. I. Vorontsova, J. E. Hall, T. F. Schilling, Assessment of zebrafish lens nucleus localization and sutural integrity. *J. Vis. Exp.* **6**, e59528 (2019).
27. F. Chauvigné, C. Zapater, J. A. Stavang, G. L. Taranger, J. Cerdà, R. N. Finn, The pH sensitivity of Aqp0 channels in tetraploid and diploid teleosts. *FASEB J.* **29**, 2172–2184 (2015).
28. G. Weber, F. J. Farris, Synthesis and spectral properties of a hydrophobic fluorescent probe: 6-propionyl-2-(dimethylamino)naphthalene. *Biochemistry* **18**, 3075–3078 (1979).
29. G. Gunther, L. Malacrida, D. M. Jameson, E. Gratton, S. A. Sánchez, LAURDAN since Weber: The quest for visualizing membrane heterogeneity. *Acc. Chem. Res.* **54**, 976–987 (2021).
30. H. S. Thoke, S. Thorsteinsson, R. P. Stock, L. A. Bagatolli, L. F. Olsen, The dynamics of intracellular water constrains glycolytic oscillations in Saccharomyces cerevisiae. *Sci. Rep.* **7**, 16250 (2017).
31. F. Begarani, F. D'Autilia, G. Signore, A. Del Grosso, M. Cecchini, E. Gratton, F. Beltram, F. Cardarelli, Capturing metabolism-dependent solvent dynamics in the lumen of a trafficking lysosome. *ACS Nano* **13**, 1670–1682 (2019).
32. F. Fereidouni, A. N. Bader, H. C. Gerritsen, Spectral phasor analysis allows rapid and reliable unmixing of fluorescence microscopy spectral images. *Opt. Express* **20**, 12729–12741 (2012).
33. D. M. Jameson, E. Gratton, R. D. Hall, The measurement and analysis of heterogeneous emissions by multifrequency phase and modulation fluorometry. *Appl. Spectrosc. Rev.* **20**, 55–106 (1984).
34. L. Malacrida, S. Astrada, A. Briva, M. Bollati-Fogolín, E. Gratton, L. A. Bagatolli, Spectral phasor analysis of LAURDAN fluorescence in live A549 lung cells to study the hydration and time evolution of intracellular lamellar body-like structures. *Biochim. Biophys. Acta Biomembr.* **1858**, 2625–2635 (2016).
35. L. Malacrida, E. Gratton, LAURDAN fluorescence and phasor plots reveal the effects of a H2O2 bolus in NIH-3T3 fibroblast membranes dynamics and hydration. *Free Radic. Biol. Med.* **128**, 144–156 (2018).
36. H. S. Thoke, A. Tobiesen, J. Brewer, P. L. Hansen, R. P. Stock, L. F. Olsen, L. A. Bagatolli, Tight coupling of metabolic oscillations and intracellular water dynamics in Saccharomyces cerevisiae. *PLOS ONE* **10**, e0117308 (2015).
37. K. Wang, I. Vorontsova, M. Hoshino, K. Uesugi, N. Yagi, J. E. Hall, T. F. Schilling, B. K. Pierscionek, Optical development in the zebrafish eye lens. *FASEB J.* **34**, 5552–5562 (2020).
38. T. M. S. Greiling, M. Aose, J. I. Clark, Cell fate and differentiation of the developing ocular lens. *Invest. Ophthalmol. Vis. Sci.* **51**, 1540–1546 (2010).
39. L. V. Virkki, G. J. Cooper, W. F. Boron, Cloning and functional expression of an MIP (AQP0) homolog from killifish (*Fundulus heteroclitus*) lens. *Am. J. Physiol.* **281**, R1994–R2003 (2001).
40. I. Vorontsova, J. E. Hall, T. F. Schilling, N. Nagai, Y. Nakazawa, Differences in a single extracellular residue underlie adhesive functions of two zebrafish Aqp0s. *Cell* **10**, 2005 (2021).
41. J. Fels, S. N. Orlov, R. Grygorczyk, The hydrogel nature of mammalian cytoplasm contributes to osmosensing and extracellular pH sensing. *Biophys. J.* **96**, 4276–4285 (2009).

42. G. H. Pollack, Is the cell a gel—And why does it matter? *Jpn. J. Physiol.* **51**, 649–660 (2001).
43. J. Peschek, N. Braun, T. M. Franzmann, Y. Georgalis, M. Haslbeck, S. Weinkauf, J. Buchner, The eye lens chaperone α-crystallin forms defined globular assemblies. *Proc. Natl. Acad. Sci. U.S.A.* **106**, 13272–13277 (2009).
44. J. S. S. Easter, G. N. Nicola, The development of vision in the zebrafish (Danio rerio). *Dev. Biol.* **180**, 646–663 (1996).
45. T. M. S. Greiling, J. I. Clark, Early lens development in the zebrafish: A three-dimensional time-lapse analysis. *Dev. Dyn.* **238**, 2254–2265 (2009).
46. K. A. Soules, B. A. Link, Morphogenesis of the anterior segment in the zebrafish eye. *BMC Dev. Biol.* **5**, 12 (2005).
47. R. T. Mathias, G. Riquelme, J. L. Rae, Cell to cell communication and pH in the frog lens. *J. Gen. Physiol.* **98**, 1085–1103 (1991).
48. J. Gao, P. J. Minogue, E. C. Beyer, R. T. Mathias, V. M. Berthoud, Disruption of the lens circulation causes calcium accumulation and precipitates in connexin mutant mice. *Am. J. Physiol. Cell Physiol.* **314**, C492–C503 (2018).
49. J. Gao, X. Sun, F. J. Martinez-Wittinghan, X. Gong, T. W. White, R. T. Mathias, Connections between connexins, calcium, and cataracts in the lens. *J. Gen. Physiol.* **124**, 289–300 (2004).
50. J. Gao, H. Wang, X. Sun, K. Varadaraj, L. Li, T. W. White, R. T. Mathias, The effects of age on lens transport. *Invest. Ophthalmol. Vis. Sci.* **54**, 7174–7187 (2013).
51. K. L. Németh-Cahalan, K. Kalman, A. Froger, J. E. Hall, Zinc modulation of water permeability reveals that aquaporin 0 functions as a cooperative tetramer. *J. Gen. Physiol.* **130**, 457–464 (2007).
52. M. Westerfield, *The Zebrafish Book: A Guide for the Laboratory Use of Zebrafish (Danio rerio)* (University of Oregon Press, ed. 4, 2000).
53. K. M. Kwan, E. Fujimoto, C. Grabher, B. D. Mangum, M. E. Hardy, D. S. Campbell, J. M. Parant, H. J. Yost, J. P. Kanki, C.-B. Chien, The Tol2kit: A multisite gateway-based construction kit for Tol2 transposon transgenesis constructs. *Dev. Dyn.* **236**, 3088–3099 (2007).
54. H.-H. Hou, M. Y.-P. Kuo, Y.-W. Luo, B.-E. Chang, Recapitulation of human βB1-crystallin promoter activity in transgenic zebrafish. *Dev. Dyn.* **235**, 435–443 (2006).
55. S. Sameni, L. Malacrida, Z. Tan, M. A. Digman, Alteration in fluidity of cell plasma membrane in Huntington disease revealed by spectral phasor analysis. *Sci. Rep.* **8**, 734 (2018).
56. J. C. Bierma, K. W. Roskamp, A. P. Ledray, A. J. Kiss, C. H. C. Cheng, R. W. Martin, Controlling liquid–liquid phase separation of cold-adapted crystallin proteins from the Antarctic toothfish. *J. Mol. Biol.* **430**, 5151–5168 (2018).
57. L. Malacrida, D. M. Jameson, E. Gratton, A multidimensional phasor approach reveals LAURDAN photophysics in NIH-3T3 cell membranes. *Sci. Rep.* **7**, 9215 (2017).
58. V. Castro-Castillo, J. Gajardo, C. Sandoval-Altamirano, E. Gratton, S. Sanchez, L. Malacrida, G. Gunther, CAPRYDAA, an anthracene dye analog to LAURDAN: A comparative study using cuvette and microscopy. *J. Mater. Chem. B* **8**, 88–99 (2020).
59. F. Sena, M. Sotelo-Silveira, S. Astrada, M. A. Botella, L. Malacrida, O. Borsani, Spectral phasor analysis reveals altered membrane order and function of root hair cells in Arabidopsis dry2/sqe1-5 drought hypersensitive mutant. *Plant Physiol. Biochem.* **119**, 224–231 (2017).
60. L. Malacrida, E. Gratton, D. M. Jameson, Model-free methods to study membrane environmental probes: A comparison of the spectral phasor and generalized polarization approaches. *Methods Appl. Fluoresc.* **3**, 019601 (2015).
61. M. Pagano, K. Gauvreau, *Principles of Biostatistics* (Duxbury, ed. 2, 2000).
62. I. Vorontsova, A. Vallmitjana, B. Torrado, T. Schilling, J. Hall, E. Gratton, L. Malacrida, *ZebraFishACDAN_Data_Code* (Figshare, 2021); https://doi.org/10.6084/m9.figshare.16900402.v2.

Acknowledgments: We are grateful to D. Jameson and P. Donaldson for reading the manuscript and for valuable suggestions. We thank I. Gehring for zebrafish husbandry and assistance in generating and maintaining the Aqp0 mutant lines. We thank J. Bierma and R. Martin for providing the crystallin sample. **Funding:** This work was supported, in part, by grants NIH P41-GM103540, NIH P50-GM076516, NIH R01-EY05661, and R01-EY031587. A.V. was supported by the Balsells Fellowship from the Generalitat de Catalunya. L.M. is supported by PEDECIBA, by the Agencia Nacional de Investigación e Innovación (ANII) grant FCE_3_2018_1_149047, by FOCEM (Fondo para la Convergencia Estructural del Mercosur; COF 03/11), and as Imaging Scientist by grant number 2020-225439 from the Chan Zuckerberg Initiative DAF, an advised fund of Silicon Valley Community Foundation. **Author contributions:** I.V., A.V., and L.M. designed experiments. I.V., A.V., B.T., and L.M. carried out experiments. I.V. and A.V. analyzed the data. A.V. wrote software for data analysis. I.V., A.V., B.T., and L.M. wrote the manuscript. All authors corrected the manuscript. **Competing interests:** The authors declare that they have no competing interests. **Data and materials availability:** All data needed to evaluate the conclusions in the paper are present in the paper and/or the Supplementary Materials. All data and code are available for download in a public repository (*62*).

Submitted 17 May 2021
Accepted 23 December 2021
Published 16 February 2022
10.1126/sciadv.abj4833